USGS Award Number: G10AP00025 & G10AP00026

Collaborative Research with Tufts University and University of Alaska Fairbanks: Application of Satellite Data for Post-liquefaction Reconnaissance

Term Covered: 1 January 2010 to 31 December 2010

PIs: Laurie G. Baise and Rudiger Gens

Thomas Oommen[1], Laurie G. Baise[2], Rudiger Gens[3], Anupma Prakash[4], and Ravi P. Gupta[5]

[1]*Department of Geological and Mining Engineering and Sciences, Michigan Technological University, Houghton, MI 49931, USA*
[2]*Department of Civil and Environmental Engineering, Tufts University, Medford, MA 02155, USA*
[3]*Alaska Satellite Facility, Geophysical Institute, University of Alaska, Fairbanks, AK 99775, USA*
[4]*Geophysical Institute, University of Alaska Fairbanks, Fairbanks, AK 99775, USA*
[5]*Department of Earth Sciences, Indian Institute of Technology - Roorkee, Roorkee 247667, India*

April 7, 2011

1 Abstract

Earthquake induced liquefaction have caused extensive structural and lifeline damage around the world. Documenting these instances of liquefaction is extremely important to help earthquake engineers better evaluate design procedures, and enhance their understanding of the liquefaction process. Currently, after an earthquake event, field-based mapping of liquefaction remains sporadic and limited due to inaccessibility, and difficulties in identifying and mapping large aerial extents. Alternatively, researchers have used change detection with remotely sensed pre- and post-event satellite images to map earthquake induced damage. However, general change detection is only a first step in developing effective strategies for documenting liquefaction due to the inherent difficulty in differentiating the changes that have occurred from various natural and earthquake induced processes between the pre- and post-event dates.

We hypothesize that as liquefaction occurs in saturated granular soils due to an increase in pore pressure which often results in excess water rising to the surface, liquefaction induced terrain changes should have an associated increase in soil moisture with respect to the surrounding non-liquefied regions, and spectral bands that are sensitive to soil moisture content can be used to identify areas that demonstrate liquefaction effects. We test our hypothesis using change detection with pre- and post-event thermal and tasseled cap wetness images derived from available Landsat ETM$^+$ for the 2001 Bhuj earthquake, in India. The tasseled cap wetness image is directly related to the soil moisture content, whereas the thermal image is inversely related to it. Results verify our hypothesis and indicate that the liquefaction zones have an associated increase in soil moisture with respect to the surrounding non-liquefied regions. The change detection of the tasseled cap transform wetness image helped to delineate earthquake induced liquefaction areas. These areas corroborated well with liquefaction areas mapped in the field.The extent of liquefaction varied within and between the geomorphological units, which we believe can be attributed to differences in the soil moisture retention capacity within and between the geomorphological units. Good baseline information on surface material composition is therefore very important for the success of future efforts in mapping liquefied areas. In addition, the coarser spatial resolution of the thermal band image resulted in only identifying the larger liquefaction features and therefore limited its application in documenting the earthquake induced liquefaction effects in its entirety. In conclusion, we recommend using change detection of tasseled cap transform wetness images for the identification of liquefaction features immediately after an earthquake. Further work will be needed to incorporate effects of different terrain, more impervious cover, etc..

2 Introduction

Historically, liquefaction-related ground failures have caused extensive structural and lifeline damage around the world. Recent examples of these effects include the damage produced during the 2001 Bhuj-India, 2010 Haiti, 2010, and 2011 New Zealand earthquakes. It is observed from these earthquakes, that the occurrence of co-seismic liquefaction, and thus the distribution of liquefaction related damage, is generally restricted to areas that contain low-density, saturated, near-surface ($<$40 feet depth) granular sediments that are found in regions prone to seismic ground motions exceeding a specified threshold level. Documenting earthquake induced liquefaction is extremely important for developing case history data sets of liquefaction occurrence/non-occurrence. Recent

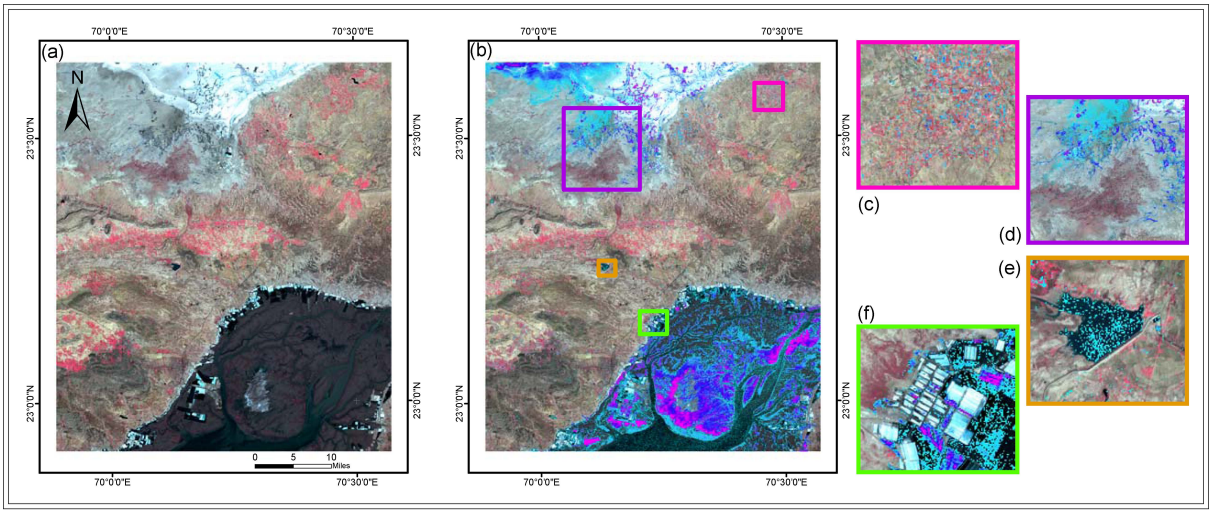

Figure 1: (a) Pan sharpened post event Std FCC of Landsat ETM$^+$ (b) Overlay of the change detection from bands 4, 2, and 3 on Figure 1a. Several different changes such as (c) changes in vegetation, (d) liquefaction related changes, (e) changes to inland water body, and (f) changes in buildings are observed from the change detection map.

work by Oommen *et al.* (2011) has shown that the bias in existing liquefaction occurrence/non-occurrence datasets can adversely affect the ability to develop accurate probabilistic liquefaction models. Thus, with improved and more complete liquefaction case history data sets, earthquake professionals will be able to improve on existing semi-empirical prediction methods, enhance their understanding of liquefaction processes, and identify limitations in emergency response and recovery.

Currently, after an earthquake event, the damage induced by the earthquake in general and liquefaction induced damages in specific are documented by reconnaissance teams (Rathje and Adams, 2008). However, large earthquakes such as the 2001 Bhuj Earthquake (Magnitude = 7.6), which shook 70% of the country, killed 19727 people and made 600,000 people homeless, pose a great challenge to field reconnaissance teams attempting to document the liquefaction effects due to (a) inaccessibility to sites immediately after the event, (b) short life of liquefaction failures, (c) difficulties in mapping the aerial extent of the failure, (d) incomplete coverage, and (e) lack of resources. Therefore, the results of field reconnaissance efforts after an earthquake event are often incomplete and biased by factors such as population density, accessibility, media coverage, urbanization etc.

Satellite remote sensing involves imaging the surface of the earth in various spectral bands at different spatial and temporal resolutions. Operational satellite remote sensing provides an unbiased record of events. Researchers have used pre- and post-earthquake images to map earthquake induced damages (Eguchi *et al.*, 2010; Gupta *et al.*, 1995; Huyck *et al.*, 2006; Kayen *et al.*, 2006; Kohiyama and Yamazaki, 2005; Mansouri *et al.*, 2005; Rathje *et al.*, 2006, 2005). These images are often used to aid the reconnaissance teams in identifying earthquake induced damages (Hisada *et al.*, 2005; Huyck *et al.*, 2005). The current approach of computer-based processing of these images to support reconnaissance efforts falls into two categories: (1) use of pre- and post-earthquake data to identify change, and (2) use of only post-earthquake imagery to identify damage. The limitation of the former approach of developing change detection maps form pre- and post-earthquake

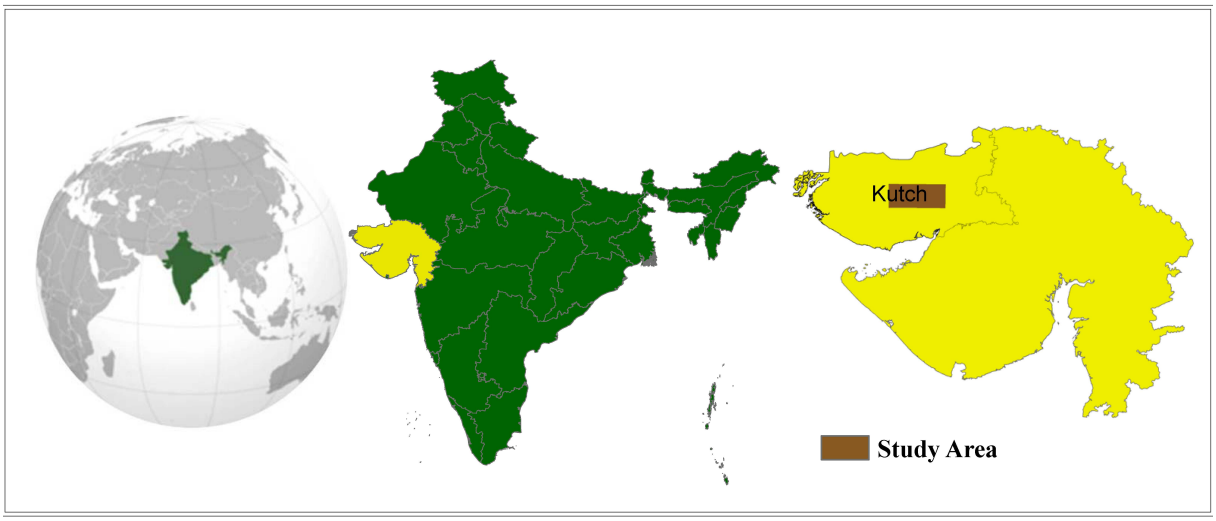

Figure 2: Study area map showing its location in the Kutch region, in the state of Gujarat in the western part of India.

image to document liquefaction is that differentiating the change in the image between the two dates based on the causative mechanism is difficult. In other words, in these change detection maps identifying liquefaction induced damages from other earthquake changes or non-earthquake changes (e.g. seasonal vegetation changes) becomes challenging and often practically impossible (Fig. 1). Hence, a general change detection map is only a first step in developing effective field reconnaissance strategies for liquefaction related data collection. The latter approach of thematic classification using only the post-earthquake image needs sufficient training instances for the supervised classification. The training instances of liquefaction induced damages are only obtained from the field reconnaissance efforts. Therefore, neither approach sufficiently aids the field reconnaissance teams in documenting liquefaction induced damages.

The objective of this research is to propose and verify an alternate method of using satellite remote sensing for aiding the reconnaissance team in identifying liquefaction induced damages. We hypothesize that as liquefaction occurs in saturated granular soils due to an increase in pore pressure which often results in vertical propagation of water, the liquefaction induced terrain changes should have an associated increase in soil moisture with respect to the surrounding non-liquefied regions. The increase in soil moisture affects the spectral signature in spectral bands that are sensitive to soil moisture such as Thermal Infrared (TIR) and Shortwave Infrared (SWIR). Additionally, components from special transforms, such as the Tasseled Cap Transform wetness component could potentially be suitable for identifying areas that have undergone earthquake induced liquefaction. We test our hypothesis using satellite imagery and field data obtained from Kutch region, in the state of Gujarat, western India (Figure 2).

3 Study Area

On 26 Jan 2001, the Kutch region recorded one of the most deadly earthquakes to strike India in its history. This intraplate earthquake, popularly known as the Bhuj Earthquake, had its epicenter

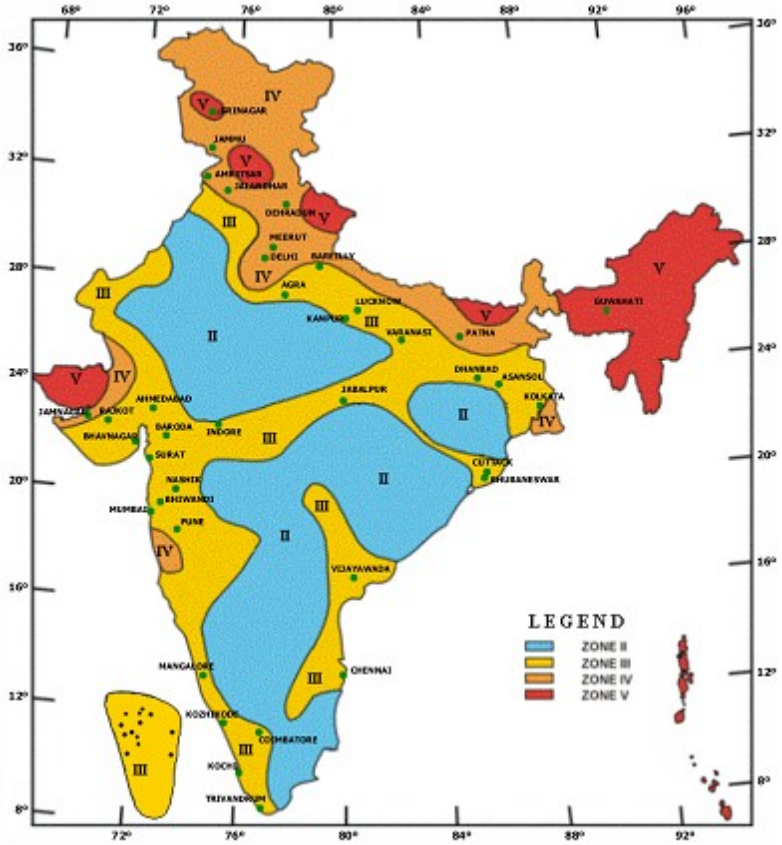

Figure 3: Seismic zoning map of India showing the distribution of the five different seismic zones across the country. It is noted that Kutch is the only region that is far from the Himalayan plate-boundary region and still has the highest seismic risk (zone v) (Source: Institute of Seismological Research- Government of India).

250 miles away from the boundary of the Indian plate and 620 miles away from the boundary of the Himalayan plate (Rastogi, 2004). The Kutch region forms a crucial geodynamic part of the western continental margin of the Indian subcontinent, and is designated zone V (Fig. 3) in the seismic zoning map of India having the highest earthquake risk of Modified Mercalli (MM) intensity IX or greater. The Indian Standard (IS) code assigns a zone factor of 0.36, which indicates that the Maximum Credible Earthquake (MCE) within this zone could generate an effective peak horizontal ground accelerations of 0.36 g. It is noted from Figure 3 that Kutch is the only region outside the plate-boundary region of the Himalayas that is designated with Zone V.

After the Bhuj earthquake, widespread appearance of water bodies, sand boils, and channels were reported by several reconnaissance teams and by local people in the Kutch region. The reconnaissance teams have identified some of these as liquefaction and cited that the accessibility to several regions of the affected area was poor particularly due to earthquake induced damages (Bilham, 2001; Mohanty *et al.*, 2001; Narula and Choubey, 2001; Ramakrishnan *et al.*, 2006; Saraf *et al.*, 2002; Singh *et al.*, 2002). The Indian remote sensing satellite (IRS-1C) with its Wide Field Sensor (WiFS) acquired an image 90 minutes after the 2001 Bhuj earthquake (26 Jan, 8:46am). This acquisition captured real time effects of earthquake. Using the IRS data and field investigations, both Saraf *et al.* (2002) and Ramakrishnan *et al.* (2006) illustrated that remote sensing can

Table 1: Details on the available satellite datasets from the study area.

Satellite/Sensor	Spectral Res. (microns)	Band	Spatial Res. (m)	Pre-event Acquisition Date	Post-event Acquisition Date
Landsat/ETM$^+$	0.45 - 0.9	VNIR: 4 bands	30	05- Nov-2000	09-Feb-2001
	1.55 - 2.35	SWIR: 2 bands	30	08- Jan-2001	
	10.4 - 12.5	TIR: 1 band	60		
	0.52 - 0.9	PAN: 1 band	15		

provide a synoptic view and analysis of the terrain changes caused by the earthquake. In this study, we use satellite images acquired by the NASA Landsat Enhanced Thematic Mapper to further address the use of satellite imagery in capturing liquefaction surface effects after an earthquake..

The study area (Kutch region) bears many geological similarities to the Mississippi Valley in the Central United States, which contains the New Madrid seismic zone (Gomberg and Schweig, 2002). Lessons learned from the Bhuj earthquake studies can be readily applied to other areas such as the Mississippi Valley. Large damaging earthquakes are rare in intraplate settings like Kutch and New Madrid and hence, each intraplate earthquake provides us a unique opportunity to make incremental advances in our ability to assess and understand the hazards posed by such events. Furthermore, both these regions have flatter topography, negating the need to correct the satellite data for varying local angle of incidence and thus varying reflectance and back-scattering behavior. The topographical simplicity of the Kutch region and the available datasets makes it an ideal site to validate our hypothesis and establish the potential of satellite remote sensing for post-earthquake field liquefaction reconnaissance planning. The boundary conditions of the new approach can be verified on more complex uneven terrains in the future.

4 Data and Methodology

To test our hypothesis that the remotely sensed images that are sensitive to soil moisture can be used for identifying earthquake induced liquefaction, we used two pre-event and one post-event Landsat ETM$^+$ image. Table 1 provides the details on the Landsat datasets used in this study, their acquisition date, and the spatial resolution. We evaluate the sensitivity of the thermal band and the tasseled cap transform wetness component of the Landsat image to soil moisture and its applicability in mapping earthquake induced liquefaction. The application of the thermal band is an indirect approach to assess the soil moisture. On vegetated and unvegetated soils, evaporation and transpiration increase as the moisture content rises. When soils are moist, the latent heat fluxes increase because of the greater absorption of water, which in turn decreases the sensible heat. The inverse of this phenomenon is observed in dry soils (Eltahir, 1998; Vicente-Serrano *et al.*, 2004). A case study of the application of thermal infrared remote sensing for soil moisture estimation using Landsat data has been presented by Shih and Jordan (1993). Shih and Jordan (1993) selected two sites in Florida for their research; one at Yelvington Farm of the Agricultural research and Education Center in Hastings and the other at Lee and Collier Counties. Soil samples for the

verification of the remote sensing data were collected and analyzed using gravimetric analysis. Shih and Jordan (1993) conclude that thermal infrared response was inversely related to the soil moisture condition. The field data provided a coefficient of correlation (r) of 0.84 between the surface temperature and soil moisture content.

In this study, the applicability of the thermal remote sensing in identifying the increase in soil moisture due to earthquake induced liquefaction is carried out by change detection of pre- and post-event Landsat ETM$^+$ thermal images using an image differencing approach. In order to account for the seasonal changes in moisture content between the pre- and post-event date, we assume that the seasonal changes in the November-January (pre-event) images are same as the January-February images (pre- and post-event). Further, to correct for the sesonal changes we subtract from the image difference of the pre- and post-event image the image difference from the pre-event images only.

The thermal bands in the Landsat image have a much coarser spatial resolution compared to the visible and near-infrared bands. To map the earthquake induced liquefaction areas at a finer spatial resolution, we found the Landsat ETM$^+$ tasseled cap transform wetness image very effective. The tasseled cap transformation is a useful tool to convert the spectral reflectance to physical scene characteristics and was originally developed for understanding important phenomena of crop development in spectral space (Crist and Cicone, 1984; Kauth and Thomas, 1976). The technique utilizes a Gram-Schmidt sequential orthogonal transformation. The initial inspiration for tasseled cap transformation was derived from (Crist and Cicone, 1984; Kauth and Thomas, 1976). The difference between tasseled cap and PCA is that while PCA places an a priori order on the principal directions in the data, the Gram-Schmidt approach allows the user to choose the order of the calculation based on a physical interpretation of the image. In this study, we use the tasseled cap transformation coefficients for Landsat ETM$^+$ reflectance developed by Huang *et al.* (2002). This transformation converts the Landsat ETM$^+$ band (bands 1-5, 7) reflectance into six axes, of which three major axes correspond to physical characteristics such as brightness, greenness, and wetness. We make use of the pre- and post-event Landsat ETM$^+$ image tasseled cap transform wetness axes to evaluate the change in wetness between the two dates. In order to account for the seasonal changes in the wetness between the two dates, similar assumptions and steps that were followed for the thermal image were carried out for the wetness image also.

The earthquake induced liquefaction mapped using the Landsat ETM$^+$ thermal image and the tasseled cap transform wetness image is compared and validated with the liquefaction instances mapped by Singh *et al.* (2002). Singh *et al.* (2002) mapped these instances immediately after the 2001 Bhuj earthquake by remote sensing and extensive field work and reported liquefaction associated damages such as cracking, water-logging, and sand boils (Singh *et al.*, 2002). The following subsections provide the fundamental principles of the steps that we have followed for the image processing and change detection and how these steps are relevant to this work.

4.1 Digital Number to Radiance and Reflectance

The use of satellite remote sensing to map objects or features on the surface of the earth is based on the concept that different objects reflect energy differently in various parts of the electromagnetic spectrum. On a satellite image, this reflected energy is represented as a Digital Number (DN). The DN depends upon the calibration parameters and radiometric resolution of the satellite sensors. The optimum detection of objects in an image requires that the data be expressed in physical units,

such as radiance or reflectance, where radiance is the variable directly measured by the sensor which is the sum of amount light observed from the target object which includes the light scattered or absorbed from the atmosphere (Pandya *et al.*, 2002; Srinivasulu and Kulkarni, 2003). Radiance has units of watts/square meter/steradian. On the other hand, reflectance has no units and it is the ratio of the amount of light striking a target to the amount of light leaving a target.

The DN values of the Landsat ETM$^+$ sensors were converted to spectral radiance using the following equation from Chander *et al.* (2009):

$$L_\lambda = L_{min\lambda} + \frac{L_{max\lambda} - L_{min\lambda}}{Q_{\text{calmax}}} \cdot Q_{\text{cal}} \tag{1}$$

where L_λ is the top of the atmosphere spectral radiance, $L_{min\lambda}$ and $L_{max\lambda}$ are the minimum and maximum spectral radiance values of the satellite sensor corresponding to the gain settings at the time of acquisition, Q_{calmax} is the maximum possible DN value, which is 255 for the Landsat ETM$^+$ sensors, and Q_{cal} which is the calibrated DN.

The spectral radiance values of the Landsat ETM$^+$ bands 1-5 & 7 are further converted from spectral radiance to spectral reflectance. The spectral reflectance is computed with the following equation:

$$\rho_{\text{p}} = \frac{\pi \cdot L_\lambda \cdot d^2}{ESUN_\lambda \cdot cos\theta_s} \tag{2}$$

where ρ_p is the unitless planetary reflectance, L_λ is the radiance, d is the Earth-Sun distance in astronomical units, $ESUN_\lambda$ is the mean solar exoatmospheric irradiances, and θ_s is the solar zenith angle in degrees.

4.2 Radiance to Temperature

The energy emitted from the Earth's surface in the thermal infrared spectrum (3-15 μm) enables calculation of the radiant temperature using Planck's law. In the past, researchers have analyzed the applicability of satellite derived surficial temperature for studying both surficial and sub-surficial characteristics (Prakash and Gupta, 1998, 1999; Prakash *et al.*, 1995; Saraf *et al.*, 1995; Zhang *et al.*, 2004). We use the pre- and post-event Landsat ETM$^+$ band-6 image to calculate the top of the atmosphere radiant temperature for study area. The Landsat ETM$^+$ measured spectral radiance is converted to the temperature using the Planck's radiation equation:

$$T = \frac{C_2}{\lambda ln[(\tau_\lambda \epsilon_\lambda C_1 \lambda^{-5}/\pi L_\lambda) + 1]} \tag{3}$$

where $C_1 = 2\pi hc$, $C_2 = hc/k$, L_λ is the spectral radiance in W.m^{-2}.ster^{-1}.μm^{-1}, h is the Planck's constant 6.626x10^{-34}, k is the Boltzmann's constant 1.380x10^{-23} JK^{-1}, T is temperature in K, c is the speed of light 2.998x10^8 ms^{-1}, τ_λ is the atmospheric transmittance, and ϵ_λ is the spectral emissivity.

The above equation can be simplified for Landsat ETM$^+$ as:

$$T = \frac{K_2}{ln\left(\frac{K_1}{L_\lambda} + 1\right)} - 273.15 \tag{4}$$

where K_1= 666.09 mW/cm^2/sr/μm, K_2 = 1260.56 mK, and T is the temperature in ^{o}C.

4.3 Tasseled Cap Transformation

In this study, we use the tasseled cap transformation coefficients for Landsat ETM$^+$ reflectance developed by Huang *et al.* (2002). Huang *et al.* (2002) developed this transformation using several hundred points of field data of soil, impervious surface, dense vegetation, and moisture content. The field data were used to rotate the principal axes obtained from PCA by preserving its orthogonality. This transformation converts the Landsat ETM$^+$ band (bands 1-5, 7) reflectance into six axes of which three major axes correspond to physical characteristics such as brightness, greenness, and wetness. We make use of the pre- and post-event Landsat ETM$^+$ image tasseled cap transform wetness axes to evaluate the increase in wetness between the two dates.

4.4 Change Detection

One of the important applications of satellite remote sensing is to detect changes occurring on the surface of the Earth. Change detection methods could be broadly categorized as either supervised or unsupervised according to the nature of the data processing technique applied (Lu *et al.*, 2004). The former is based on a supervised classification method, which requires the availability of a ground truth in order to derive a suitable training set for the learning process of the classifier, whereas, the latter approach performs change detection by making a direct comparison of the pre- and post-event images. The unsupervised change detection is mainly carried out using one of the following: 1) image differencing, 2) image ratioing, 3) change vector analysis, or 4) principal component analysis. The various change detection techniques have been reviewed by (Coppin and Bauer, 1996; Deer, 1995; Jensen *et al.*, 1997; Mouat *et al.*, 1993; Prakash and Gupta, 1998; Serpico and Bruzzone, 1999; Singh, 1989; Yuan *et al.*, 1999). In this study, the unsupervised change detection is performed by image differencing as follows:

$$D(x) = I_2(x) - I_1(x) \tag{5}$$

where $D(x)$ is the difference image, $I_2(x)$ is the post-event image, and $I_1(x)$ is the pre-event image. The image differencing results in positive and negative values in areas of surface change and zero values in areas of no change (Sohl, 1999). The difference image often produces a distribution that is approximately Gaussian in nature with pixels of no change distributed around the mean and changed pixels distributed in the tails of the distribution (Gupta, 2003). A necessary pre-processing step before image differencing is normalization or standardization to reduce the inherent variability between the multitemporal datasets (pre- and post-event image) (Warner and Chen, 2001). The process substantially reduces the inter scene variability due to different imaging conditions. In normalization, the image minimum is subtracted from the pixel value and divided by the data range, whereas in standardization the image mean is subtracted from the pixel value and divided by the standard deviation. In this study, image standardization was applied before image differencing. A change class map was developed from the difference image by simply thresholding it according to the following decision rule:

$$B(x) = \begin{cases} 1, & \text{if } |D(x) > \tau \\ 0, & \text{otherwise} \end{cases} \tag{6}$$

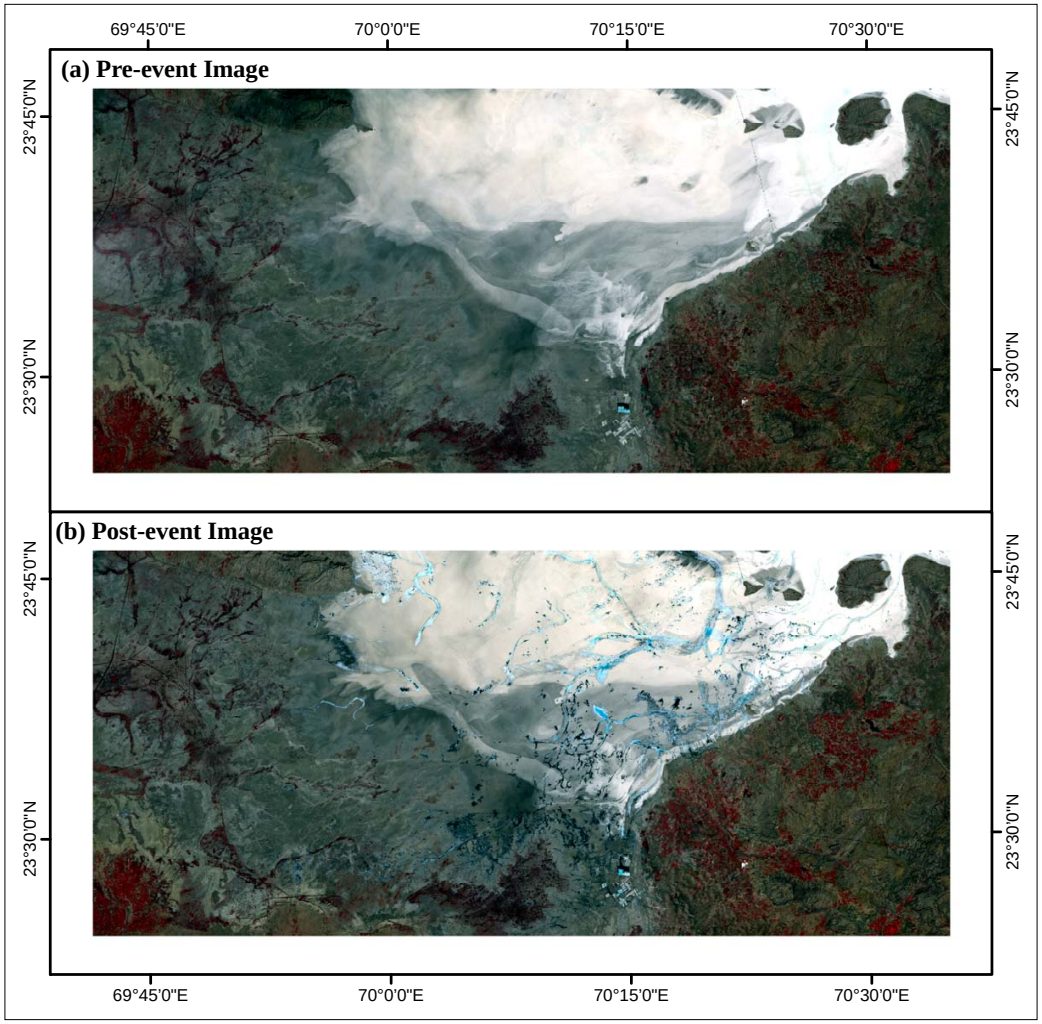

Figure 4: Comparison of the Landsat ETM$^+$ pre- and post-event image (a) standard false color composite of the pre-event (08-Jan-2001) image (b) standard false color composite of the post-event (09-Feb-2001) image. The vegetation is seen as red.

where $B(x)$ denotes the change mask, and τ denotes the threshold. The minimum number of change classes is two. In this study we used 11 change classes with 5 positive change classes, 5 negative change classes, and one no change class with the thresholds being evenly spaced between -1 and +1.

5 Analysis Results and Discussions

Landsat ETM$^+$ pre- and post-event standard false color composite shows (Figure 4) that the study area has scanty vegetation and a generally flat topography. The scantily vegetated area (red tones in Figure 4) are mostly towards the south-east and south-west corners of the study area. Even though the study area has mostly flat topography, Roy and Merh (1977) identified two major geomorphologic units in the area: (1) the bet zone (bets meaning "raised land"), and (2) the trench zone. The bet zone comprises of slightly elevated patches of grassland along with intervening channels and it

is mostly composed of fine micaceous sand and silt with clay intercalation (Rajendran and Rajendran, 2001). The scantily vegetated areas identified towards the south-east and south-west corners of the study area (Figure 4) can be identified as bet zones.

The trench zone mostly consists of salty lowland that is seasonally marshy. The northern part of the study area, which is part of the trench zone is adjacent to an inlet to the Arabian Sea that floods annually. When the salt water from the flooding dries, a white salty crust is left behind (Gomberg and Schweig, 2002). The bright white signature observed towards the north of the study area in the Landsat ETM$^+$ pre- and post-event standard false color composite image (Figure 4) demonstrates the presence of the salty crust. Several changes in the trench zone are visible between the two date images.

The radiant temperature (in °C) was estimated for the different images using Landsat ETM$^+$ thermal band. The estimated temperature within the study area ranged from 23.5 to 44.5, -4.4 to 32.8, and 16.8 to 47.1°C for November, January, and February images, respectively. Comparing the November pre-event temperature image (Figure 5a) with the February post-event temperature image (Figure 5b) shows the bet zone is much warmer than the trench zone in both the pre- and post-event images.

It is evident from the post-event image that there are pockets within the trench zone that have significant reduction in temperature compared to its surrounding. The Figure 5b inset provides a zoom of a region that has significant reduction in temperature compared to the neighboring pixels. Figure 5c presents the image difference between the pre- and post-event thermal image corrected for the seasonal changes. In Figure 5c blue represents cooler regions where the temperature has decreased, whereas red represents warmer regions where the temperature has increased in the post-event image relative to the pre-event image. Since the surface temperature is inversely related to the moisture content, the areas with decreased temperature could possibly represent areas of increased moisture content. Further, Figure 5c is overlaid by regions within the study area that have extreme reduction in temperature which is defined as areas where the change in temperature magnitude is $>$ -1.5 standard deviation.

Figure 6 presents a profile A - A' (location of profile line is shown in Figure 5b inset) along the pre- and post-event temperature images and the image difference. The pre-event temperature profile is pretty constant along the profile. However, the post-event and the image difference temperature profiles show a significant reduction in temperature (about 8°C) towards the midpoint of the profile. It is important to note that this reduction in temperature is localized and not observed in the pre-event image. This localized reduction in temperature observed in the post-event image could be from the increase in surface moisture caused by the earthquake induced liquefaction.

To investigate the applicability of higher resolution images in capturing the increase in soil moisture due to liquefaction, we also analyzed the tasseled cap wetness image. The Landsat ETM$^+$ tasseled cap wetness image has a 30m spatial resolution whereas, the temperature image has a 60m resolution. Figure 7 presents the tasseled cap wetness image for the pre- and post-event dates obtained using the Landsat ETM$^+$ tasseled cap transform. In the pre-event tasseled cap wetness image (Figure 7a) the difference in wetness between the trench and bet zone is as distinct as observed in the temperature image. However, in the post-event tasseled cap wetness image (Figure 7b) several localized regions are observed in the trench zone with increased wetness. Figure 7c presents the image difference between the pre- and post-event tasseled cap wetness image corrected for the seasonal changes. For the seasonal correction, the procedure that was adopted for the temperature image was also followed for the tasseled cap wetness image. Since the wetness is directly corre-

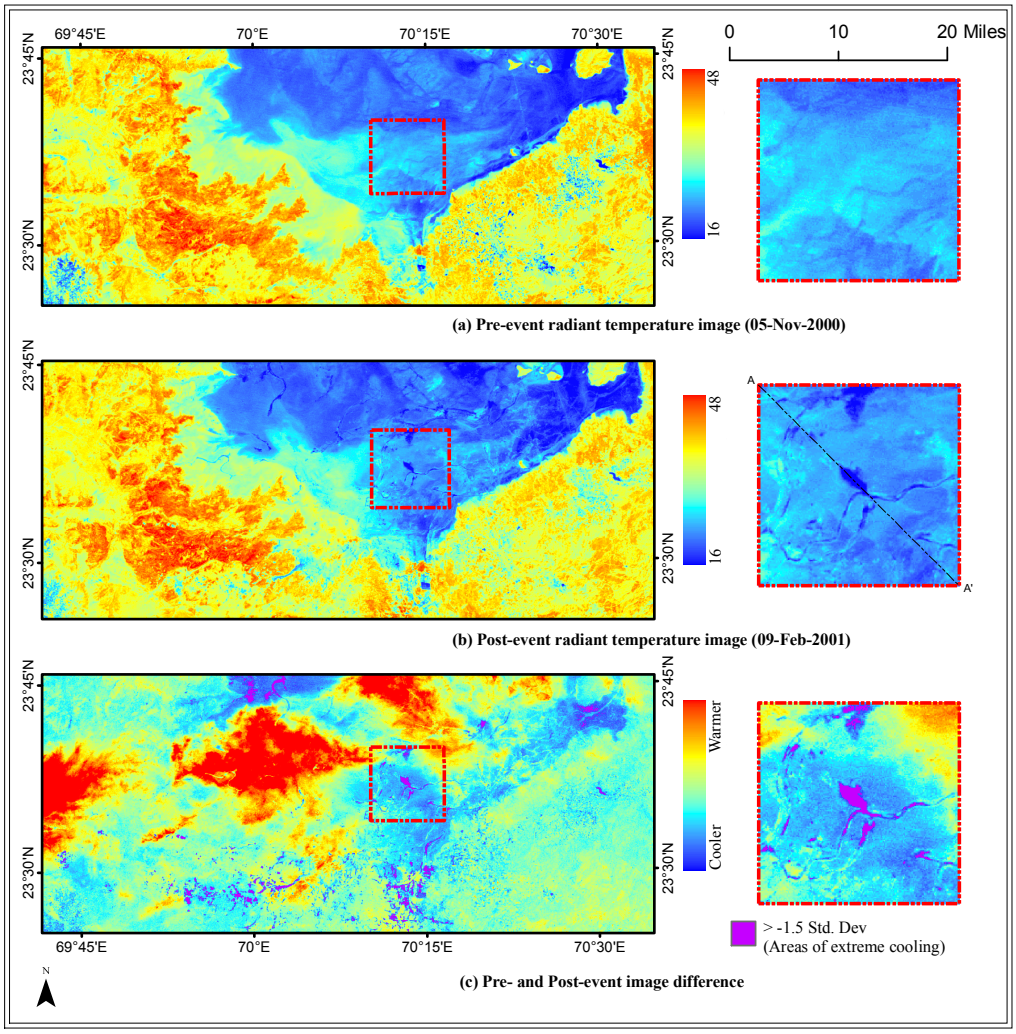

Figure 5: Landsat ETM$^+$ radiant temperature image in degree celsius (°C) (a) pre-event (05-Nov 2000), (b) post-event (09-Feb 2001), (c) pre- and post-event radiant temperature image difference corrected for the seasonal changes and overlaid by regions of extreme decrease in temperature, i.e. $>$ -1.5 standard deviation filtered (inset shows zoom of the region within the study area).

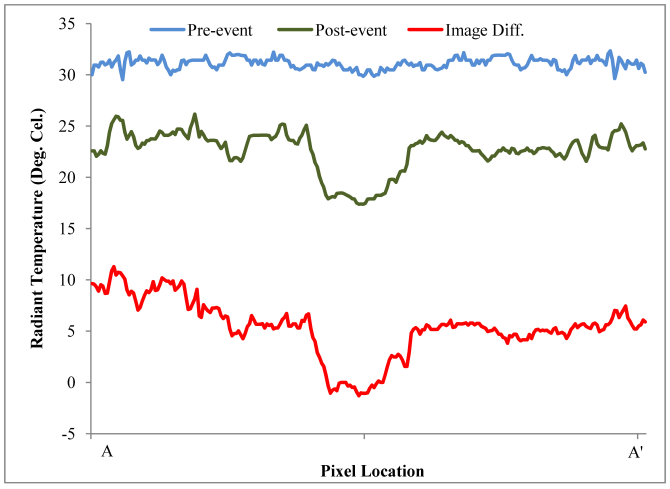

Figure 6: Landsat ETM$^+$ radiant temperature profile along section A-A' (profile line is shown in Figure 5b inset).

lated with moisture content, the areas with increased wetness could possibly represent areas where the moisture content has increased. Figure 7c is also overlaid by regions within the study area that have extreme increase in wetness which is defined as areas where the change in wetness magnitude is $>$ -1.5 standard deviation. There are much more instances of extreme wetness change compared to the extreme temperature change between the pre- and post-event image. It is likely that the localized increase in soil moisture observed in the post-event image are smaller features and are not captured in a coarse spatial resolution image or the change in temperature in these features are not easily distinguishable from the surrounding.

Figure 8 presents a profile A - A' (location of profile line is shown in Figure 7b inset) along the pre- and post-event tasseled cap wetness images and the image difference. The pre-event tasseled cap wetness profile is generally consistent along the profile similar to the pre-event temperature image profile (Figure 6). However, the post-event and the image difference temperature profiles show a significant increase in tasseled cap wetness along the profile. However, towards the center of the profile the increase in wetness is several pixels long and indicates that it is a large feature, which also appears distinctly in the temperature image profile (Figure 6). This indicates that the fewer observation of extreme temperature changes in the temperature profile (Figure 6) compared to the extreme tasseled cap wetness changes is due to the limitations in the spatial resolution of the temperature image.

Finally, we compare the extreme changes observed from the Landsat ETM$^+$ radiant temperature and the tasseled cap wetness to the liquefaction instances mapped by Singh *et al.* (2002) (Figure 9). These instances were mapped immediately after 2001 Bhuj earthquake by remote sensing and extensive field work. Figures 9b and c show the overlay of the extreme radiant temperature and extreme wetness respectively on the liquefaction instances mapped by Singh *et al.* (2002). In Figure 9b most of the extreme temperature changes correspond with the liquefaction instances mapped by Singh *et al.* (2002). However, only a few instances of liquefactions mapped by Singh *et al.* (2002) are actually identified as extreme changes from the temperature image. This could be because of the coarser spatial resolution of temperature image. Figure 9c shows that extreme wet-

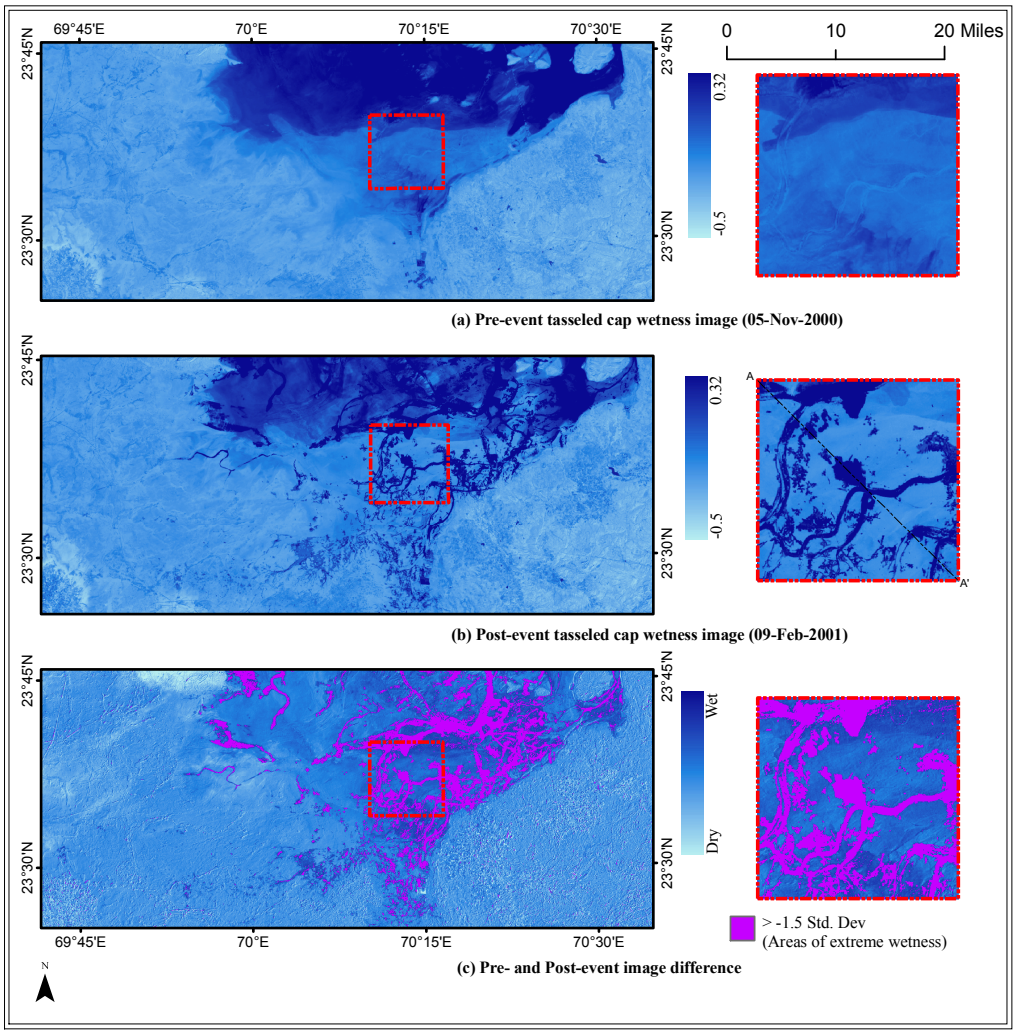

Figure 7: Landsat ETM$^+$ tasseled cap wetness image (a) pre-event (05-Nov 2000), (b) post-event (09-Feb 2001), (c) pre- and post-event tasseled cap wetness image difference corrected for the seasonal changes and overlaid by regions of extreme increase in wetness, i.e. $>$ + 1.5 standard deviation filtered (inset shows zoom of the region within the study area).

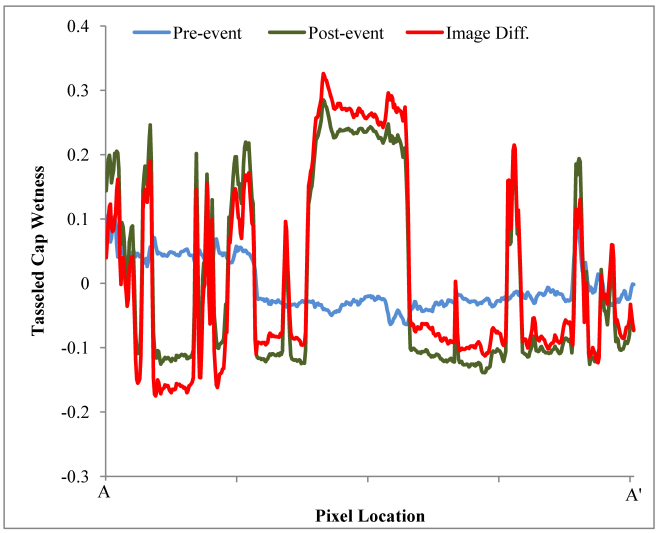

Figure 8: Landsat ETM$^+$ tasseled cap wetness profile along section A-A' (profile line is shown in Figure 7b inset).

ness changes correspond well with the liquefaction instances mapped by Singh *et al.* (2002). The correspondence between the extreme wetness change and liquefaction instances is best towards the center of the study area whereas the extreme changes over-predicts the liquefaction instances towards the north and under-predicts towards the south.

In the pre-event tasseled cap wetness image (Figure 7a) surface moisture levels increased within the trench zone towards the northern part of the study area compared to the rest of the trench zone. The liquefaction instances mapped by Singh *et al.* (2002) in the study area towards the south are on the bet zone whereas the instances of liquefaction mapped in the central and northern part of the study area are in the trench zone. The reason why the liquefaction instances within the bet zone are not identified from the extreme changes in wetness is possibly because the soil moisture retention capacity of these zone might be different from the trench zone. Therefore, incorporating the soil moisture retention capacity of the various geomorphological units and filtering the extreme changes based on these will be critical when using remote sensing to map earthquake induced liquefaction.

6 Conclusions and Limitations

In this study, we evaluate the applicability of satellite remote sensing for mapping the surficial expression of earthquake induced liquefaction. We hypothesize that as liquefaction occurs in saturated granular soils due to increase in pore pressure and that water will tend to propagate vertically, the liquefaction related terrain changes should have an associated increase in soil moisture with respect to the surrounding non-liquefied regions. We test this hypothesis using Landsat ETM$^+$ thermal and tasseled cap wetness transform image by image differencing of the pre- and post-event image. We further filter the extreme changes in the image difference and compare with the liquefaction instances mapped by Singh *et al.* (2002). We draw the following conclusions from this study:

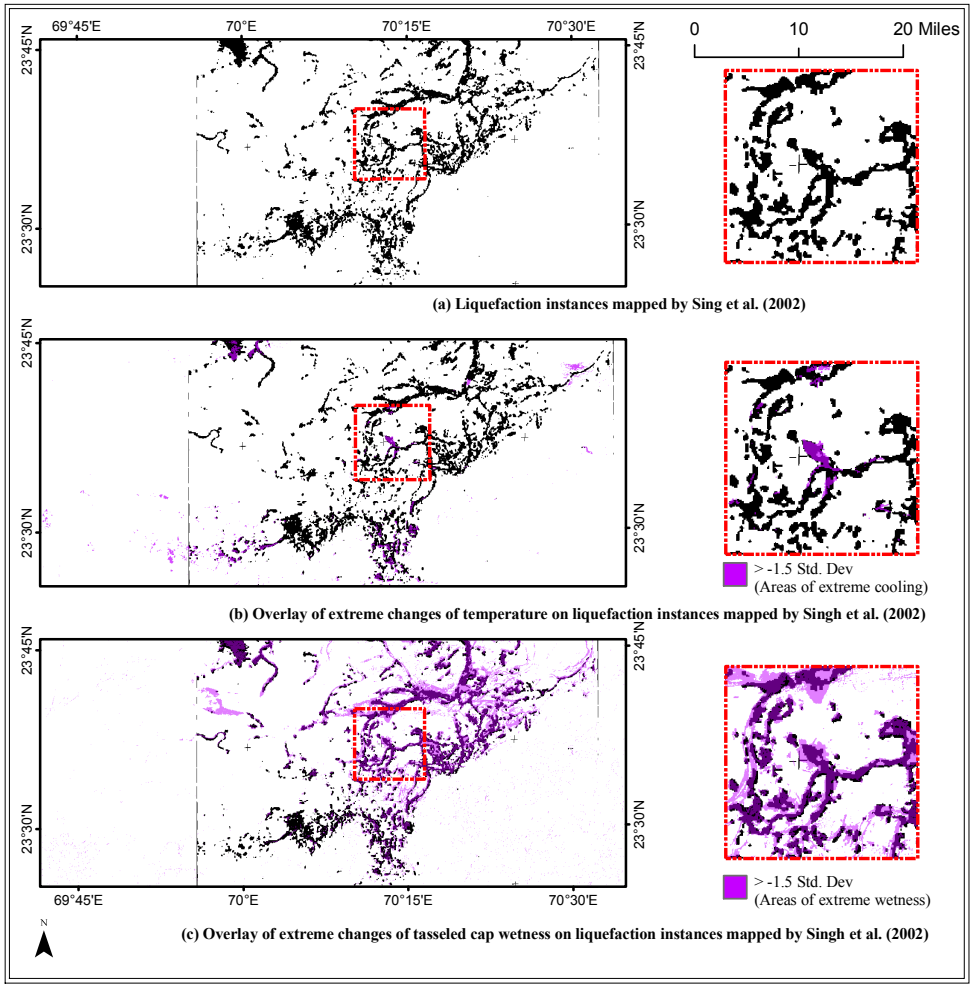

Figure 9: Extreme changes in temperature and tasseled cap wetness overlaid on the liquefaction instances from 2001 Bhuj earthquake mapped by Singh *et al.* (2002) (a) liquefaction instances mapped by Singh *et al.* (2002), (b) overlay of extreme changes from radiant temperature image difference, (c) overlay of extreme changes from tasseled cap wetness image difference (inset shows zoom of the region within the study area).

- The seasonally corrected image difference of the pre- and post-event Landsat ETM$^+$ tasseled cap transform wetness image shows promise in mapping the surficial expression of earthquake induced liquefaction and has a higher resolution than the thermal image (30 m versus 60 m).

- The high correlation of the extreme changes filtered from the tasseled cap wetness image with liquefaction instances mapped by Singh *et al.* (2002) verifies our hypothesis that the liquefaction zones have an associated increase in soil moisture with respect to the surrounding non-liquefied regions.

- The correlation of the estimates of liquefaction from tasseled cap wetness with liquefaction instances mapped by Singh *et al.* (2002) was higher in the trench zone compared to the bet zone.

- The difference in the estimates of liquefaction instances mapped from tasseled cap wetness change within and outside the trench zone indicate that the associated increase in soil moisture due to liquefaction is related to the soil moisture retention capacity of the geomorphological unit and its inclusion could possibly improve the estimates.

- The results indicate that the use of remotely sensed data, sensitive to soil moisture, can be an integral part in regionally documenting earthquake induced liquefaction failures and strategizing post-earthquake response and reconnaissance.

- The seasonally corrected image difference of the pre- and post-event Landsat ETM$^+$ thermal band image indicates that its spatial resolution limits its application for detailed mapping of liquefaction effects. The thermal images identify larger liquefaction features but not the numerous smaller features.

- An obvious limitation for this approach to map liquefaction is that meteorological factors, such as a heavy rain event prior to post-event image acquisition, would erase surficial expressions of liquefaction.

7 Recommendations for Future Work

The current study area does not have high topography nor dense vegetations. In the future, the applicability of this approach in varying conditions of topography and vegetation needs to be verified. Furthermore, the moisture retention capacity of the geomorphological unit and the initial moisture condition should be incorporated to improve the estimates of liquefaction effects.

References

Bilham, R. (2001). 26 January 2001 Bhuj earthquake, Gujarat, India URL http://cires.colorado.edu/~bilham/Gujarat2001.html.

Chander, G., B. Markham, and D. Helder (2009). Summary of current radiometric calibration coefficients for Landsat MSS, TM, ETM+, and EO-1 ALI sensors, *Remote Sensing of Environment* **113**(5), 893–903.

Coppin, P., and M. Bauer (1996). Digital change detection in forest ecosystem with remote sensing imagery, *Remote Sensing of the Environment* **13**, 207–234.

Crist, E. P., and R. C. Cicone (1984). A physically-based transformation of thematic mapper data - the TM tasseled cap, *IEEE Trans. on Geosciences and Remote Sensing* **GE-22**(3), 252–263.

Deer, P. (1995). Digital change detection techniques in remote sensing, *DSTO Tech. Report* p. 44p.

Eguchi, R. T., S. P. Gill, S. Ghosh, W. Svekla, B. J. Adams, G. Evans, J. Toro, K. Saito, and R. Spence (2010). The January 12, 2010 Haiti earthquake: A comprehensive damage assessment using very high resolution areal imagery, *8th International Workshop on Remote Sensing for Disaster Management, Tokyo Institute of Technology, Tokyo, Japan.* .

Eltahir, E. A. B. (1998). A soil moisture-rainfall feedback mechanism, *Water Resources Research* **34**(4), 765–776.

Gomberg, J., and E. Schweig (2002). East meets Midwest: An earthquake in India helps hazard assessment in the Central United States, *U.S. Geological Survey Fact Sheet* (FS-007-02).

Gupta, R. P. (2003). *Remote Sensing Geology*, 2nd Edition, Heidelberg: Springer-Verlag.

Gupta, R. P., R. Chander, A. K. Tewari, and A. K. Saraf (1995). Remote-sensing delineation of zones susceptible to seismically induced liquefaction in the Ganga plains, *Journal of the Geological Society of India* **46**(1), 75–82.

Hisada, Y., A. Shibayama, and M. R. Ghayamghamian (2005). Building damage and seismic intensity in Bam city from the 2003 Iran, Bam, earthquake .

Huang, C., B. Wylie, L. Yang, C. Homer, and G. Zylstra (2002). Derivation of a tasselled cap transformation based on Landsat 7 at satellite reflectance, *International Journal of Remote Sensing* **23**(8), 1741–1748.

Huyck, C., B. Adams, S. Cho, H. C. Chung, and R. Eguchi (2005). Towards rapid citywide damage mapping using neighborhood edge dissimilarities in very high-resolution optical satellite imagery application to the 2003 Bam, Iran earthquake, *Earthquake Spectra* **21**(S1), 255–266.

Huyck, C., M. Matsuoka, Y. Takahashi, and T. Vu (2006). Reconnaissance technologies used after the 2004 Niigata-ken Chuetsu, Japan, earthquake, *Earthquake Spectra* (22), 133–145.

Jensen, J., K. Rutchey, M. Koch, and H. J. (1997). *Principles of change detection using digital remote sensor data*, Cambridge University Press, Cambridge.

Kauth, R. J., and G. S. Thomas (1976). The tasseled cap a graphic description of the spectral temporal development of agricultural crops as seen in Landsat, *Proceedings on the Symposium on Machine Processing of Remotely Sensed Data, West Lafayette, Indiana (West Lafayette, Indiana: LARS, Purdue University)* pp. 41–51.

Kayen, R., R. Pack, J. Bay, S. Sugimoto, and H. Tanaka (2006). Ground-lidar visualization of surface and structural deformation of the Niigata Ken Chuetsu, 23 october 2004, earthquake, *Earthquake Spectra* **22**, 147–162.

Kohiyama, M., and F. Yamazaki (2005). Damage detection for 2003 Bam, Iran earthquake using terra-aster satellite imagery, *Earthquake Spectra* **21**(S1), 267–274.

Lu, P. D., E. B. Mausel, and E. Moran (2004). Change detection techniques, *International Journal of Remote Sensing* **25**(12), 2365–2407.

Mansouri, B., M. Shinozuka, C. Huyck, and B. Houshmand (2005). Earthquake-induced change detection in the 2003 Bam, Iran earthquake by complex analysis using Envisat ASAR data, *Earthquake Spectra* (21), 275–284.

Mohanty, K., K. Maiti, and S. Nayak (2001). Change detection techniques, *GIS@Development* **v**(3), URL www.GISdevelopment.net.

Mouat, D. A., G. C. Mahin, and J. Lancaster (1993). Remote sensing techniques in the analysis of change detection, *Geocarto International* **2**, 39–50.

Narula, P. L., and S. K. Choubey (2001). Macroseismic surveys for the Bhuj (India) earthquake of 26 January, 2001 URL http://www.Nicee.org/NICEE/Gujarat/narula.htm.

Oommen, T., L. G. Baise, and R. Vogel (2011). Sampling bias and class imbalance in maximum likelihood logistic regression, *Mathematical Geosciences* **43**(1), 99–120.

Pandya, M. R., R. Singh, K. R. Murali, P. N. Babu, A. S. Kirankumar, and V. K. Dadhwal (2002). Bandpass solar exoatmospheric irradiance and rayleigh optical thickness of sensors on board Indian remote sensing satellites-1B, -1C, -1D, and P4, *IEEE Transactions on Geoscience and Remote Sensing* **40**(3), 714–718.

Prakash, A., and R. P. Gupta (1998). Land-use mapping and change detection in a coal mining area - a case study in the jharia coalfield, india, *International Journal of Remote Sensing* **19**(3), 391–410.

Prakash, A., and R. P. Gupta (1999). Surface fires in Jharia coalfield, India their distribution and estimation of area and temperature from tm data, *International Journal of Remote Sensing* **20**(10), 1935–1946.

Prakash, A., R. G. S. Sastry, R. P. Gupta, and A. K. Saraf (1995). Estimating the depth of buried hot features from thermal IR remote sensing data - a conceptual approach, *International Journal of Remote Sensing* **16**(13), 2503–2510.

Rajendran, C. P., and K. Rajendran (2001). Characteristics of deformation and past seismicity associated with the 1819 Kutch earthquake, northwestern India, *Bulletin of the seismological society of America* **91**(3), 407–426.

Ramakrishnan, D., K. K. Mohanty, S. R. Nayak, and R. V. Chandran (2006). Mapping the liquefaction induced soil moisture changes using remote sensing technique: An attempt to map the earthquake induced liquefaction around Bhuj, Gujarat, India, *Geotechnical and Geological Engineering* **24**(6), 1581–1602.

Rastogi, B. K. (2004). Damage due to the m-w 7.7 Kutch, India earthquake of 2001, *Tectonophysics* **390**(1-4), 85–103.

Rathje, E., R. Kayen, and K. S. Woo (2006). Remote sensing observations of landslides and ground deformation from the 2004 Niigata Ken Chuetsu earthquake, *Soils and Foundations* **46**(6), 831–842.

Rathje, E. M., and B. J. Adams (2008). The role of remote sensing in earthquake science and engineering: Opportunities and challenges, *Earthquake spectra* **24**(2), 471–492.

Rathje, E. M., M. Crawford, K. Woo, and A. Neuenschwander (2005). Damage patterns from satellite images from the 2003 Bam, Iran earthquake, *Earthquake Spectra* **21**(S1), 295–307.

Roy, B., and S. S. Merh (1977). *Geomorphology of the Rann of Kutch and climatic changes, in Ecology and Archaeology of Western India*, Concept Publishing Company, Anand Nagar, Delhi, India.

Saraf, A. K., A. Prakash, S. Sengupta, and R. P. Gupta (1995). Landsat TM data for estimating ground temperature and depth of subsurface coal fire in the Jharia coalfield,India, *International Journal of Remote Sensing* **16**(12), 2111–2124.

Saraf, A. K., A. Sinvhal, H. Sinvhal, P. Ghosh, and B. Sarma (2002). Satellite data reveals 26 January 2001 Kutch earthquake-induced ground changes and appearance of water bodies, *International Journal of Remote Sensing* **23**(9), 1749–1756.

Serpico, S., and L. Bruzzone (1999). *Change detection*, World Scientific Publishing, Singapore.

Shih, S., and J. Jordan (1993). Use of Landsat Thermal-IR data and gis in soil-moisture assessment, *Journal of Irrigation and Drainage Engineering* **119**(5), 868–879.

Singh, A. (1989). Digital change detection techniques using remotely sensed data, *International Journal of Remote Sensing* **10**(6), 989–1003.

Singh, R. P., S. Bhoi, and A. K. Sahoo (2002). Changes observed in land and ocean after Gujarat earthquake of 26 January 2001 using IRS data, *International Journal of Remote Sensing* **16**(23), 3123–3128.

Sohl, T. L. (1999). Change analysis in the United Arab Emirates: an investigation of techniques, *Photogrammetric Engineering and Remote Sensing* **65**(4), 475–484.

Srinivasulu, J., and A. V. Kulkarni (2003). Estimation of spectral reflectance of snow from IRS-1D LISS-iii sensor over the Himalayan terrain, *Journal of Earth System Science* **113**(1), 117–128.

Vicente-Serrano, S., X. Pons-Fernandez, and J. Cuadrat-Prats (2004). Mapping soil moisture in the Central Ebro river valley (Northeast Spain) with Landsat and NOAA satellite imagery: a comparison with meteorological data, *International Journal of Remote Sensing* **25**(20), 4325–4350.

Warner, T. A., and X. Chen (2001). Normalization of Landsat thermal imagery for the effects of solar heating and topography, *International Journal of Remote Sensing* **22**(5), 773–788.

Yuan, D., C. Elvidge, and L. R.S. (1999). *Multispectral Methods for Land Cover Change Analysis*, Taylor & Francis Ltd, 1 Gunpowder Square, London.

Zhang, G., P. Robertson, and R. Brachman (2004). Estimating liquefaction-induced lateral displacements using the Standard Penetration Test or Cone Penetration Test, *Journal of Geotechnical and Geoenvironmental Engineering* **8**(130), 861–871.

8 Bibliography of all publications resulted from this work

T Oommen, L G Baise, R Gens, A Prakash, R P Gupta (2011) Documenting earthquake-induced liquefaction using satellite remote sensing sensitive to soil moisture. Bulletin of the Seismological Society of America (In review)

T Oommen, L G Baise, R Gens, A Prakash, R P Gupta (2010) Applying Satellite Remote Sensing to Document Liquefaction Failures. Seismological Research Letters, 81(2): 253-283

T Oommen, L G Baise, R Gens, A Prakash, R P Gupta (2010) Documenting liquefaction failures using satellite. 8th International Workshop on Remote Sensing for Disaster Management, Tokyo, Japan.